

Deep CNNs Meet Global Covariance Pooling: Better Representation and Generalization

Qilong Wang, *Member, IEEE*, Jiangtao Xie, Wangmeng Zuo, *Senior Member, IEEE*,
Lei Zhang, *Fellow, IEEE*, and Peihua Li, *Member, IEEE*

Abstract—Compared with global average pooling in existing deep convolutional neural networks (CNNs), global covariance pooling can capture richer statistics of deep features, having potential for improving representation and generalization abilities of deep CNNs. However, integration of global covariance pooling into deep CNNs brings two challenges: (1) robust covariance estimation given deep features of high dimension and small sample; (2) appropriate use of geometry of covariances. To address these challenges, we propose a *global Matrix Power Normalized COVariance (MPN-COV) Pooling*. Our MPN-COV conforms to a robust covariance estimator, very suitable for scenario of high dimension and small sample. It can also be regarded as power-Euclidean metric between covariances, effectively exploiting their geometry. Furthermore, a global Gaussian embedding method is proposed to incorporate first-order statistics into MPN-COV. For fast training of MPN-COV networks, we propose an iterative matrix square root normalization, avoiding GPU unfriendly eigen-decomposition inherent in MPN-COV. Additionally, progressive 1×1 and group convolutions are introduced to compact covariance representations. The MPN-COV and its variants are highly modular, readily plugged into existing deep CNNs. Extensive experiments are conducted on large-scale object classification, scene categorization, fine-grained visual recognition and texture classification, showing our methods are superior to the counterparts and achieve state-of-the-art performance.

Index Terms—Global covariance pooling, matrix power normalization, deep convolutional neural networks, visual recognition.



1 INTRODUCTION

DEEP convolutional neural networks (CNNs) have achieved great success in many computer vision tasks, especially in visual recognition [1], [2], [3], [4], [5]. However, the existing deep CNN architectures generate the final representations using a simple, first-order, global average pooling (GAP), neglecting richer statistical information inherent in deep feature map, which may limit the representation ability in large-scale scenarios as well as generalization ability on challenging small-scale datasets [6], [7], [8]. To overcome this problem, one possible solution is to replace first-order GAP by some more powerful modeling methods.

Compared with first-order pooling methods, covariance (second-order) pooling is able to capture richer statistics of features so that it can generate more informative representations [9], [10]. Since covariance matrices are symmetric positive definite (SPD) matrices whose space forms a Riemannian manifold, their geometric structure should be favorably considered for realizing the full potential [9], [10]. In the seminal paper of [9], Tuzel et al. propose to utilize covariance matrices for representing regular regions

of images, and employ affine invariant Riemannian metric (AIRM) [11] to measure the distances between covariance matrices. Differently, Carreira et al. [10] present an O_2P method, where second-order non-central moments are used to model free-form regions of images, and Log-Euclidean Riemannian metric (LERM) [12] is adopted as the distance measure. In the classical shallow architectures [10], [13], covariance pooling combining with hand-crafted features (e.g., SIFT [14] and L^2EMG [15]) achieves much better recognition performance than first-order ones, as well as is superior to the popular Bag-of-Visual-Words (BoVW) models [16], [17].

In terms of above discussion, a question naturally arises: *Can we exploit global covariance pooling to improve the representation and generalization abilities of deep CNN architectures?* Ionescu et al. [18] make the first attempt to integrate O_2P [10] with matrix logarithm normalization into deep CNNs (called Deep O_2P). They establish the theory and practice of backpropagation method which enables end-to-end learning of CNN involving non-linear structural matrices. A parallel work is the bilinear CNN (B-CNN) [19] model, which performs outer product pooling of output features of the last convolution layers from two CNN models, producing non-central moment when the two CNNs are identical. But differently, B-CNN performs element-wise power normalization followed by ℓ_2 -normalization for the resulting SPD matrices rather than matrix logarithm in Deep O_2P .

Although above global covariance pooling (GCP) methods [18], [19] have been studied for obtaining feasible improvement in deep architectures, there still exist two challenges in combining GCP with deep CNNs. The first one is robust covariance estimation. The dimensions of output features of the last convolution layers in deep CNNs usually are very high (e.g., 256 in AlexNet [1], 512 in VGG-VD [2]

- Q. Wang was with the School of Information and Communication Engineering, Dalian University of Technology, Liaoning 116024, China and he is presently with the College of Intelligence and Computing, Tianjin University, Tianjin 300350, China. (E-mail: qlwang@tju.edu.cn)
- J. Xie and P. Li are with the School of Information and Communication Engineering, Dalian University of Technology, Liaoning 116024, China. (E-mail: jiangtaoxie@mail.dlut.edu.cn; peihuali@dlut.edu.cn)
- W. Zuo is with the School of Computer Science and Technology, Harbin Institute of Technology, Harbin, 150001, China. (E-mail: cswmzuo@gmail.com)
- L. Zhang is with the Department of Computing, The Hong Kong Polytechnic University, Hung Hom, Hong Kong. (E-mail: cszhang@comp.polyu.edu.hk)
- P. Li is the corresponding author. (E-mail: peihuali@dlut.edu.cn)

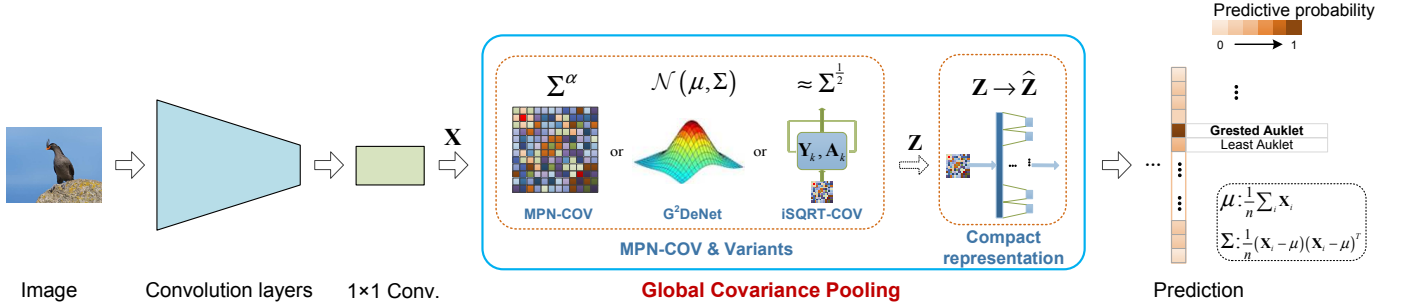


Fig. 1. Overview of deep convolutional neural networks with the proposed global Matrix Power Normalized COVariance (MPN-COV) Pooling and its variants. The MPN-COV block is inserted after the last convolution layer to summarize the second-order statistics of convolution activations as global representations. Several variants are proposed to refine MPN-COV: firstly, a global Gaussian embedding (G^2DeNet) method is presented to incorporate additional first-order information; then, an iterative matrix square root normalization (iSQRT-COV) method is proposed for fast training of the network, and finally, the progressive 1×1 convolutions and group convolution are introduced to compact covariance representations.

and 2048 in ResNet [4]), but the feature number is small (< 200). Under such a scenario of high dimension and small sample size, it is well-known that the sample covariance obtained by the classical maximum likelihood estimation (MLE) is not robust [20], [21]. Furthermore, recent studies [13], [22] have shown that robust covariance estimation leads to performance improvement in the case of high dimension and small sample size. The second challenge is how to make favorable use of geometry lying in the space of covariance matrices. DeepO₂P [18] exploits geometry of covariances using LERM [12], but our experiments (Section 4.2.2) show that LERM brings side effect for covariance matrices in above scenarios. B-CNN [19] simply regards the space of covariances as a Euclidean space, discarding its geometric structure. Furthermore, neither DeepO₂P [18] nor B-CNN [19] is concerned with robust covariance estimation.

To address the above two challenges, this paper proposes a global Matrix Power Normalized COVariance (MPN-COV) Pooling for deep CNNs. Different from the existing GCP [18], [19], our MPN-COV can account for robust covariance estimation: MPN-COV with power larger than zero conforms to the general shrinkage principle of eigenvalues [23], [24] and that with power of $1/2$ can be derived explicitly via maximum likelihood estimator regularized by von Neumann divergence [22]. As a result, MPN-COV is very suitable for the scenario of high dimension and small sample size. Meanwhile, MPN-COV can be regarded as power-Euclidean metric [25] between covariance matrices, which is closely connected to the LERM [12]. As such, our MPN-COV approximately yet effectively exploits geometry of covariance matrices, concurrently circumventing the downside of LERM in deep architecture. Furthermore, our MPN-COV paradigm can accommodate first-order (mean) information through embedding a global Gaussian distribution into deep CNNs, where a Gaussian is uniquely identified as a square root SPD matrix based on Lie group theory [15].

For forward/backward propagation, our MPN-COV needs to compute matrix power, which heavily depends on eigen-decomposition (EIG) or singular value decomposition (SVD). However, implementation of EIG or SVD is limitedly supported on CUDA platform (significantly slower than their CPU counterparts [18], [26]), so existing methods [18], [27], [28] implement them on CPU. As such, GPUs with powerful parallel ability have to be interrupted and

await CPUs with limited parallel ability, restricting concurrency and throughput, and so slowing down network training, especially for multi-GPU configuration. To handle this problem, we propose a trainable, iterative matrix square root normalized covariance pooling (iSQRT-COV)¹ based on Newton-Schulz iteration [29], which involves only matrix multiplication, very suitable for parallel implementation on GPU. By introducing pre-normalization and post-compensation layers, iSQRT-COV can be trained by deriving the gradients associated with the involved non-linear layers based on matrix backpropagation theory [18]. Our iSQRT-COV significantly speeds up training of MPN-COV networks, particularly on multi-GPU configuration.

The output features of deep CNNs usually are of high dimension, which results in much larger size of covariance representations, suffering from high computational and memory costs. To compact covariance representations, we propose to exploit progressive 1×1 convolutions and group convolution [30] to obtain smaller size representations with little performance loss. The proposed MPN-COV and its variants can be readily inserted into existing deep CNN architectures in an end-to-end manner. Fig. 1 illustrates deep CNNs with our proposed MPN-COV and its variants. Finally, we conduct experiments on a variety of visual recognition tasks, including large-scale object classification, scene categorization, fine-grained visual recognition, and texture classification. This paper summarizes and extends our preliminary works [27], [28], [31], and the contributions are summarized as follows:

- We propose an global Matrix Power Normalized COVariance (MPN-COV) pooling to improve the representation and generalization abilities of deep CNNs. Moreover, we make an attempt to analyze the mechanisms underlying MPN-COV, which addresses the challenges of robust covariance estimation and Riemannian geometry of covariances.
- We propose several variants to refine MPN-COV. Firstly, we propose a Gaussian embedding method to properly incorporate additional first-order information. Then, a trainable iterative matrix square root

¹ The matrix square root normalization is a special case of MPN-COV where the power is $1/2$ that usually performs best among all values of power (Refer to experiments in Sec. 4.2.1).

normalization method is proposed for fast training of MPN-COV networks. Additionally, the progressive 1×1 convolutions and group convolution are introduced to reduce size of covariance representations. These variants make our MPN-COV more systematic and practical.

- The proposed MPN-COV networks are implemented on different deep learning platforms, and the complete code will be released to open source repository. We write C++ code based on NVIDIA cuBLAS and Matlab using MatConvNet package [32]. Meanwhile, we implement our fast MPN-COV (iSQRT-COV) using PyTorch package.
- Extensive evaluations are conducted on various visual recognition tasks, including large-scale object classification on ImageNet [33] and scene categorization on Place365 [34], fine-grained visual recognition on Birds-CUB200-2011 [35], Aircrafts [36] and Cars [37], texture classification on DTD [38] and Indoor67 [39], and iNaturalist Challenge 2018 held in FGVC5 workshop in conjunction with CVPR 2018. The results with different CNN architectures (e.g., AlexNet [1], VGG-VD [2], ResNet [4] and DenseNet [5]) show the superiority of our MPN-COV networks.

2 RELATED WORK

This section reviews the related works, which aim at improving deep CNNs through integration of trainable sophisticated pooling or encoding strategies. These methods are divided into four categories.

2.1 Deep CNNs with Global Second-order Pooling

Both DeepO₂P [18] and B-CNN [19] insert a trainable second-order non-central moment into deep CNNs, where matrix logarithm normalization and element-wise power normalization followed by ℓ_2 -normalization are performed, respectively. Going beyond B-CNN, Lin et al. [26] study the effect of different normalization methods on B-CNN, and empirically find matrix square root normalization achieves the best results. The resulting method is called improved B-CNN, where forward propagation is implemented by Newton-Schulz iteration (called modified Denman-Beavers iteration therein), while backward propagation is achieved by SVD/Lyapunov equation. The improved B-CNN shares the parallel idea with a variant of our MPN-COV, i.e., iSQRT-COV. But differently, both forward and backward propagations of our iSQRT-COV are performed based on Newton-Schulz iteration, much more efficient than improved B-CNN. More importantly, instead of only empirical experiments in improved B-CNN, we give theoretical explanations on why matrix power normalization is effective for covariance pooling in deep architectures. Additionally, we evaluate the proposed methods on more visual recognition tasks and with more CNN architectures besides fine-grained visual recognition and VGG-VD in [26], and results show our methods outperform improved B-CNN on both large-scale and small-scale classification tasks.

2.2 Deep CNNs with Global Approximate High-order Pooling

In general, high-order pooling methods result in high-dimensional representations. Gao et al. [40] and Kong et al. [41] propose compact B-CNN and low-rank B-CNN models to reduce dimensions of covariance (second-order) representations, respectively. These methods replace exact covariances by low-dimensional approximation ones, while achieving comparable performance. Based on compact B-CNN model [40], Dai et al. [42] fuse additional first-order (mean) information by simply concatenating them. Kernel pooling [43] extends the similar idea with the compact B-CNN to approximate higher-order (number of order > 2) pooling. Sharing similar philosophy with [43], Cai et al. [44] obtain low-dimensional higher-order representations based on polynomial kernel approximation and rank-1 tensor decomposition [45], namely HIIHCA. Both kernel pooling [43] and HIIHCA [44] improve compact B-CNN by exploiting higher-order statistical information. However, all above methods consider neither robust estimation nor geometry of statistical manifold, limiting the ability of higher-order modeling.

2.3 Deep CNNs with Local Second-order Statistics

In contrary to above works exploring global second-order pooling, some researchers try to incorporate local second-order statistics into deep CNNs. Among them, Factorized Bilinear (FB) method [46] introduces an additional parametric quadratic term into linear transformation of convolution or fully-connected (FC) layers. FB can incorporate more complex non-linearity structures into deep CNNs by considering second-order interaction between information flow. Second-Order Response Transform (SORT) [47] proposes to fuse outputs of two-branch block using a second-order term (i.e., element-wise product and a sum operation), in order to increase the nonlinearity of deep CNNs as well. Obviously, these methods also discard robust estimation and geometry of second-order statistics so that they cannot make full use of capacity of second-order pooling.

2.4 Deep CNNs with Trainable BoVW Methods

In the past decades, BoVW is one of the most widely used orderless pooling methods for visual classification. Recently, some works insert high-performance BoVW methods [16], [17] as trainable structural layers into deep CNNs. Thereinto, NetVLAD [48] implements the modified vector of locally aggregated descriptors (VLAD) [16] in an end-to-end manner. FisherNet [49] accomplishes the trainable layer of simplified Fisher vector (FV) [17]. Unlike FisherNet, Li et al. [50] propose a MFAFVNet for scene categorization, which performs a deep embedded implementation of mixture of factor analyzers Fisher vector (MFA-FV) method [51]. Different from these methods, this paper proposes to integrate a global covariance pooling endowed with matrix power normalization into deep CNNs. The experimental comparisons show our methods are significantly superior to deep BoVW methods.

3 THE PROPOSED METHOD

In this section, we will introduce the proposed GCP methods for deep CNNs. We first describe our MPN-COV and the underlying mechanisms. Then, we show how to instantiate deep CNNs with our MPN-COV, and present a global Gaussian embedding method to fuse first-order information. Subsequently, we improve speed of training MPN-COV network by introducing a trainable, iterative matrix square root normalization method. Finally, progressive 1×1 convolutions and group convolution are introduced to reduce size of covariance representations.

3.1 Global Matrix Power Normalized COVariance (MPN-COV) Pooling

3.1.1 Computation of MPN-COV

Given an input feature matrix $\mathbf{X} \in \mathbb{R}^{d \times M}$ consisting of M samples with d -dimension, its sample covariance can be computed as

$$\mathbf{\Sigma} = \mathbf{X}\mathbf{J}\mathbf{X}^T, \quad \mathbf{J} = \frac{1}{M}(\mathbf{I} - \frac{1}{M}\mathbf{1}\mathbf{1}^T), \quad (1)$$

where \mathbf{I} indicates a $M \times M$ identity matrix, $\mathbf{1}$ is a M -dimension vector with all elements being one, and T denotes the matrix transpose.

The sample covariance $\mathbf{\Sigma}$ is a symmetric positive definite or semidefinite matrix, which can be factorized by eigen-decomposition (EIG) or singular value decomposition (SVD), i.e.,

$$\mathbf{\Sigma} = \mathbf{U}\mathbf{\Lambda}\mathbf{U}^T, \quad (2)$$

where $\mathbf{\Lambda} = \text{diag}(\lambda_1, \dots, \lambda_d)$ is a diagonal matrix and $\lambda_i, i = 1, \dots, d$ are eigenvalues arranged in non-increasing order; $\mathbf{U} = [\mathbf{u}_1, \dots, \mathbf{u}_d]$ is an orthogonal matrix whose column \mathbf{u}_i is the eigenvector corresponding to λ_i . Through EIG or SVD, we can compute matrix power as follows:

$$\mathbf{Z} \triangleq \mathbf{\Sigma}^\alpha = \mathbf{U}\text{diag}(f(\lambda_1), \dots, f(\lambda_d))\mathbf{U}^T. \quad (3)$$

Here α is a positive real number and $f(\lambda_i)$ is power of the eigenvalues

$$f(\lambda_i) = \lambda_i^\alpha. \quad (4)$$

In this paper, the operation as described in Eq. (3) is called *MPN-COV*, which is inserted after the last convolution layer of deep CNNs to collect second-order statistics of the output features (i.e., \mathbf{X}) as global representations. Next, we describe the mechanisms underlying MPN-COV in terms of robust covariance estimation and usage of geometry.

3.1.2 Robust Covariance Estimation

Assuming \mathbf{X} are sampled from a Gaussian distribution, the covariance $\mathbf{\Sigma}$ of \mathbf{X} can be estimated by optimizing the following objective function based on the MLE:

$$\arg \min_{\mathbf{\Sigma}} \log |\mathbf{\Sigma}| + \text{tr}(\mathbf{\Sigma}^{-1}\mathbf{S}), \quad (5)$$

where $\mathbf{S} = \mathbf{X}\mathbf{J}\mathbf{X}^T$ is sample covariance, $|\cdot|$ indicates matrix determinant and $\text{tr}(\cdot)$ means trace of matrix. The solution to the MLE (5) is the sample covariance, i.e., $\mathbf{\Sigma} = \mathbf{S}$. However, it is well known that MLE is not robust when data is of high

dimension with small sample size [20], [21]. This scenario is just what our covariance pooling faces: in most of the existing deep CNNs [2], [3], [4], [5], the output features (i.e., \mathbf{X}) of last convolution layer have less than 200 samples of dimension larger than 512, so the sample covariances are always ill-conditioned, rendering robust estimation critical.

For robust estimation of covariances in the case of high-dimension and small sample size, the general principle is shrinkage of eigenvalues of the sample covariances for counteracting the ill-conditioning of covariance matrices [23], [24]. Besides, some researchers propose various regularized MLE methods for robust covariance estimation (see [52] and references therein). Notably, our MPN-COV closely conforms to the shrinkage principle [23], [24], i.e., shrinking the largest sample eigenvalues and stretching the smallest ones. Moreover, MPN-COV can be deemed as a regularized MLE, namely vN-MLE [22]:

$$\arg \min_{\widehat{\mathbf{\Sigma}}} \log |\widehat{\mathbf{\Sigma}}| + \text{tr}(\widehat{\mathbf{\Sigma}}^{-1}\mathbf{S}) + \gamma D_{\text{vN}}(\mathbf{I}, \widehat{\mathbf{\Sigma}}), \quad (6)$$

where $\gamma > 0$ is a regularizing constant, and $D_{\text{vN}}(\mathbf{A}, \mathbf{B}) = \text{tr}(\mathbf{A}(\log(\mathbf{A}) - \log(\mathbf{B})) - \mathbf{A} + \mathbf{B})$ is matrix von-Neumann divergence. Compared with the classical MLE (5) which only includes the first two terms, the objective function of vN-MLE (6) introduces the third term, constraining the estimated covariance $\widehat{\mathbf{\Sigma}}$ be similar to the identity matrix \mathbf{I} . In [22], it has been shown that the vN-MLE outperforms other shrinkage methods [23], [24], [53] and regularized MLE method [52]. Briefly, we have

Proposition 1. MPN-COV with $\alpha = \frac{1}{2}$ is the unique solution to the vN-MLE in which $\gamma = 1$, i.e.,

$$\mathbf{\Sigma}^{\frac{1}{2}} = \arg \min_{\widehat{\mathbf{\Sigma}}} \log |\widehat{\mathbf{\Sigma}}| + \text{tr}(\widehat{\mathbf{\Sigma}}^{-1}\mathbf{S}) + D_{\text{vN}}(\mathbf{I}, \widehat{\mathbf{\Sigma}}), \quad (7)$$

where $\mathbf{\Sigma} = \mathbf{S}$.

Proposition 1 shows our MPN-COV with $\alpha = 1/2$ performs robust estimation of covariance, and experiments in Section 4.2.1 show that $\alpha = 1/2$ performs best. Details on vN-MLE can be referred to [22].

3.1.3 Approximate Usage of Geometry

Since the space of $d \times d$ covariance matrices (denoted by \mathbb{S}_d^+) forms a Riemannian manifold, geometry should be considered when distances between covariances are measured. There are mainly two kinds of Riemannian metrics, i.e., AIRM [11] and LREM [12]. The AIRM is affine-invariant, but it is computationally inefficient and coupled, not scalable to large-scale scenarios. The LERM is a similarity-invariant decoupled metric and efficient to compute, so that it is scalable to large-scale problems. Our MPN-COV can be regarded as matching covariance matrices with the Power-Euclidean (Pow-E) metric [25], which has close connection with the LERM, as presented in the following proposition:

Proposition 2. For any two covariance matrices $\mathbf{\Sigma}_1$ and $\mathbf{\Sigma}_2$, the limit of the Pow-E metric $d_\alpha(\mathbf{\Sigma}_1, \mathbf{\Sigma}_2) = \frac{1}{\alpha} \|\mathbf{\Sigma}_1^\alpha - \mathbf{\Sigma}_2^\alpha\|_F$ as $\alpha > 0$ approaches 0 equals the LERM, i.e., $\lim_{\alpha \rightarrow 0} d_\alpha(\mathbf{\Sigma}_1, \mathbf{\Sigma}_2) = \|\log(\mathbf{\Sigma}_1) - \log(\mathbf{\Sigma}_2)\|_F$.

This conclusion was first mentioned in [25] but without proof. Here we briefly prove this proposition. Note that

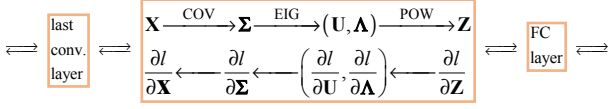


Fig. 2. Diagram of the proposed MPN-COV block.

$d_\alpha(\Sigma_1, \Sigma_2) = \left\| \frac{1}{\alpha}(\Sigma_1^\alpha - \mathbf{I}) - \frac{1}{\alpha}(\Sigma_2^\alpha - \mathbf{I}) \right\|_F$. For any covariance Σ we have $\frac{1}{\alpha}(\Sigma^\alpha - \mathbf{I}) = \mathbf{U} \text{diag}\left(\frac{\lambda_1^{\alpha-1}}{\alpha}, \dots, \frac{\lambda_d^{\alpha-1}}{\alpha}\right) \mathbf{U}^T$ based on its EIG. The identity about the limit in Proposition 2 follows immediately by recalling $\lim_{\alpha \rightarrow 0} \frac{\lambda^\alpha - 1}{\alpha} = \log(\lambda)$. Hence, the proposed MPN-COV can be viewed as approximately exploiting the Riemannian geometry of \mathbb{S}_d^+ . It seems that the LERM is better than the Pow-E metric, since the former computes the true geodesic distance but the latter one only measures it approximately. We argue that this is not the case for the scenario of deep CNNs from the perspectives of both numerical stability and distribution of eigenvalues. Detailed discussion is given in Section 4.2.2.

3.2 Global MPN-COV Pooling Neural Network

We first instantiate a global matrix power normalized covariance pooling neural network (MPN-COV-Net) by inserting our MPN-COV after the last convolution layer of deep CNNs, in place of the common GAP. The diagram of our MPN-COV block is illustrated in Fig. 2. For forward propagation, we first compute the covariance pooling of output features \mathbf{X} of the last convolution layer using Eq. (1), then we perform matrix power normalization (3). Inspired by the element-wise power normalization technique [17], we can further perform, after MPN-COV, normalization by matrix ℓ_2 -norm (M- ℓ_2) or by matrix Frobenius norm (M-Fro). The matrix ℓ_2 -norm (also known as the *spectral norm*) of a matrix Σ , denoted by $\|\Sigma\|_2$, is defined as the largest singular value of Σ , which equals the largest eigenvalue if Σ is a covariance matrix. The matrix Frobenius norm of Σ can be defined in various ways such as $\|\Sigma\|_F = (\text{tr}(\Sigma^T \Sigma))^{\frac{1}{2}} = (\sum_i \lambda_i^2)^{\frac{1}{2}}$, where λ_i are eigenvalues of Σ . Then, we have

$$f(\lambda_i) = \begin{cases} \lambda_i / \lambda_1^\alpha & \text{for MPN-COV+M-}\ell_2 \\ \lambda_i^\alpha / (\sum_k \lambda_k^{2\alpha})^{\frac{1}{2}} & \text{for MPN-COV+M-Fro} \end{cases} \quad (8)$$

For backpropagation of MPN-COV block, we need to compute the partial derivative of loss function l with respect to the input \mathbf{X} based on the methodology of matrix backpropagation [18], [54]. First of all, given $\frac{\partial l}{\partial \mathbf{Z}}$ propagated from the top fully-connected layer, we compute the derivative of $\frac{\partial l}{\partial \mathbf{U}}$ and $\frac{\partial l}{\partial \Lambda}$ based on the following chain rule:

$$\text{tr}\left(\left(\frac{\partial l}{\partial \mathbf{U}}\right)^T d\mathbf{U} + \left(\frac{\partial l}{\partial \Lambda}\right)^T d\Lambda\right) = \text{tr}\left(\left(\frac{\partial l}{\partial \mathbf{Z}}\right)^T d\mathbf{Z}\right), \quad (9)$$

where $d\mathbf{Z}$ denotes variation of matrix \mathbf{Z} . According to Eq. (3), we have $d\mathbf{Z} = d\mathbf{U}\mathbf{F}\mathbf{U}^T + \mathbf{U}d\mathbf{F}\mathbf{U}^T + \mathbf{U}\mathbf{F}d\mathbf{U}^T$, where $\mathbf{F} = \text{diag}(f(\lambda_1), \dots, f(\lambda_d))$ and $d\mathbf{F} = \text{diag}(\alpha\lambda_1^{\alpha-1}, \dots, \alpha\lambda_d^{\alpha-1})d\Lambda$. After some arrangements, we obtain

$$\begin{aligned} \frac{\partial l}{\partial \mathbf{U}} &= \left(\frac{\partial l}{\partial \mathbf{Z}} + \left(\frac{\partial l}{\partial \mathbf{Z}}\right)^T\right) \mathbf{U}\mathbf{F}, \\ \frac{\partial l}{\partial \Lambda} &= \alpha \left(\text{diag}\left(\lambda_1^{\alpha-1}, \dots, \lambda_d^{\alpha-1}\right) \mathbf{U}^T \frac{\partial l}{\partial \mathbf{Z}} \mathbf{U}\right)_{\text{diag}}, \end{aligned} \quad (10)$$

where $(\cdot)_{\text{diag}}$ denotes the matrix diagonalization. For MPN-COV+M- ℓ_2 and MPN-COV+M-Fro, $\frac{\partial l}{\partial \Lambda}$ takes respectively the following forms:

$$\begin{aligned} \frac{\partial l}{\partial \Lambda} &= \frac{\alpha}{\lambda_1} \left(\text{diag}\left(\lambda_1^{\alpha-1}, \dots, \lambda_d^{\alpha-1}\right) \mathbf{U}^T \frac{\partial l}{\partial \mathbf{Z}} \mathbf{U}\right)_{\text{diag}} \\ &\quad - \text{diag}\left(\frac{\alpha}{\lambda_1} \text{tr}\left(\mathbf{Z} \frac{\partial l}{\partial \mathbf{Z}}\right), 0, \dots, 0\right) \end{aligned} \quad (11)$$

and

$$\begin{aligned} \frac{\partial l}{\partial \Lambda} &= \frac{\alpha}{\sqrt{\sum_k \lambda_k^{2\alpha}}} \left(\text{diag}\left(\lambda_1^{\alpha-1}, \dots, \lambda_d^{\alpha-1}\right) \mathbf{U}^T \frac{\partial l}{\partial \mathbf{Z}} \mathbf{U}\right)_{\text{diag}} \\ &\quad - \frac{\alpha}{\sum_k \lambda_k^{2\alpha}} \text{tr}\left(\mathbf{Z} \frac{\partial l}{\partial \mathbf{Z}}\right) \text{diag}\left(\lambda_1^{2\alpha-1}, \dots, \lambda_d^{2\alpha-1}\right). \end{aligned} \quad (12)$$

Next, given $\frac{\partial l}{\partial \mathbf{U}}$ and $\frac{\partial l}{\partial \Lambda}$, we need to compute $\frac{\partial l}{\partial \Sigma}$ associated with Eq. (2), whose corresponding chain rule is $\text{tr}\left(\left(\frac{\partial l}{\partial \Sigma}\right)^T d\Sigma\right) = \text{tr}\left(\left(\frac{\partial l}{\partial \mathbf{U}}\right)^T d\mathbf{U} + \left(\frac{\partial l}{\partial \Lambda}\right)^T d\Lambda\right)$. Note that \mathbf{U} is an orthogonal matrix. After some arrangements, we have

$$\frac{\partial l}{\partial \Sigma} = \mathbf{U} \left(\left(\mathbf{K}^T \circ \left(\mathbf{U}^T \frac{\partial l}{\partial \mathbf{U}}\right)\right) + \left(\frac{\partial l}{\partial \Lambda}\right)_{\text{diag}} \right) \mathbf{U}^T, \quad (13)$$

where \circ denotes matrix Hadamard product. The matrix $\mathbf{K} = \{K_{ij}\}$ where $K_{ij} = 1/(\lambda_i - \lambda_j)$ if $i \neq j$ and $K_{ij} = 0$ otherwise. We refer readers to [54, Proposition 2] for in-depth derivation of Eq. (13).

Finally, given $\frac{\partial l}{\partial \Sigma}$, we derive the gradient of the loss function with respect to the input feature matrix \mathbf{X} , which has

$$\frac{\partial l}{\partial \mathbf{X}} = \left(\frac{\partial l}{\partial \Sigma} + \left(\frac{\partial l}{\partial \Sigma}\right)^T\right) \mathbf{X}\mathbf{J}. \quad (14)$$

As described above, by using the formulas of Eq. (3) and Eq. (14), our MPN-COV-Net can be trained in an end-to-end manner.

3.3 Global Gaussian Distribution Embedding Neural Network

The covariance pooling captures second-order statistics of features $\mathbf{X} = [\mathbf{x}_1, \dots, \mathbf{x}_M] \in \mathbb{R}^{d \times M}$. The first-order (mean) information of features can be introduced by modeling \mathbf{X} using a global Gaussian distribution:

$$p(\mathbf{x}) = \frac{1}{(2\pi)^{\frac{d}{2}} |\Sigma|^{\frac{1}{2}}} \exp\left(-\frac{1}{2}(\mathbf{x} - \boldsymbol{\mu})^T \Sigma^{-1}(\mathbf{x} - \boldsymbol{\mu})\right),$$

where $\boldsymbol{\mu} = \frac{1}{M} \sum_{i=1}^M \mathbf{x}_i$ and $\Sigma = \frac{1}{M} \sum_{i=1}^M (\mathbf{x}_i - \boldsymbol{\mu})(\mathbf{x}_i - \boldsymbol{\mu})^T$ are mean vector and sample covariance matrix, respectively.

It is well known that the space of multivariate Gaussians (denote by $\mathcal{G}(d)$) is a Riemannian manifold having special geometric structure [55]. The recent work [15] has made advance, showing that $\mathcal{G}(d)$ can be endowed with a Lie group structure, i.e., $\mathcal{G}(d)$ is not only a Riemannian manifold but also is a smooth group. Let $UT^+(d+1)$ be the set of all positive definite upper triangular matrices of order $d+1$ which is a Lie group, and $\Sigma^{-1} = \mathbf{L}\mathbf{L}^T$ be the Cholesky decomposition of the inverse of Σ , where \mathbf{L} is a lower triangular matrix of order d with positive diagonals. Through

$$\phi(\mathcal{N}(\boldsymbol{\mu}, \Sigma)) = \mathbf{H}_{\boldsymbol{\mu}, \mathbf{J}} \triangleq \begin{bmatrix} \mathbf{J} & \boldsymbol{\mu} \\ \mathbf{0}^T & \mathbf{1} \end{bmatrix}, \quad (15)$$

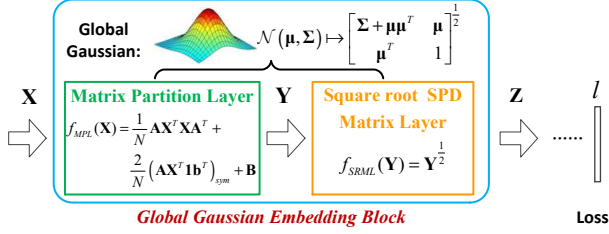


Fig. 3. Diagram of the proposed global Gaussian embedding block.

a Gaussian $\mathcal{N}(\boldsymbol{\mu}, \boldsymbol{\Sigma})$ is uniquely mapped to the matrix $\mathbf{H}_{\boldsymbol{\mu}, \mathbf{J}} \in UT^+(d+1)$, where $\mathbf{J} = \mathbf{L}^{-T}$. However, the embedding form (15) does not suit for backpropagation due to the Cholesky decomposition and matrix inverse.

The matrix $\mathbf{H}_{\boldsymbol{\mu}, \mathbf{J}}$ can be further mapped to a unique SPD matrix based on matrix polar decomposition and Lie group isomorphism. Let $\mathbf{H}_{\boldsymbol{\mu}, \mathbf{J}} = \mathbf{S}_{\boldsymbol{\mu}, \mathbf{J}} \mathbf{Q}_{\boldsymbol{\mu}, \mathbf{J}}$ be the left polar decomposition of $\mathbf{H}_{\boldsymbol{\mu}, \mathbf{J}}$, where $\mathbf{S}_{\boldsymbol{\mu}, \mathbf{J}}$ and $\mathbf{Q}_{\boldsymbol{\mu}, \mathbf{J}}$ are $(d+1) \times (d+1)$ SPD matrix and orthogonal matrix of determinant one, respectively. Then, we have

$$\psi(\mathbf{H}_{\boldsymbol{\mu}, \mathbf{J}}) = \mathbf{S}_{\boldsymbol{\mu}, \mathbf{J}} = \begin{bmatrix} \boldsymbol{\Sigma} + \boldsymbol{\mu}\boldsymbol{\mu}^T & \boldsymbol{\mu} \\ \boldsymbol{\mu}^T & 1 \end{bmatrix}^{\frac{1}{2}}. \quad (16)$$

Through the above consecutive mappings, our introduced Gaussian embedding can be represented as follows:

$$(\psi \circ \phi)(\mathcal{N}(\boldsymbol{\mu}, \boldsymbol{\Sigma})) = \begin{bmatrix} \boldsymbol{\Sigma} + \boldsymbol{\mu}\boldsymbol{\mu}^T & \boldsymbol{\mu} \\ \boldsymbol{\mu}^T & 1 \end{bmatrix}^{\frac{1}{2}}. \quad (17)$$

Readers can refer to [15] for details of mapping process. According to the embedding form in Eq. (17), we can construct our global Gaussian embedding block by decomposing it into two layers, i.e., matrix partition layer and square root SPD matrix layer. It is shown in Fig. 3, and the deep CNNs with our global Gaussian embedding block are called global Gaussian distribution embedding neural networks (G^2 DeNet).

Matrix Partition Layer We denote $\mathbf{Y} = f_{MPL}(\mathbf{X}) \triangleq \begin{bmatrix} \boldsymbol{\Sigma} + \boldsymbol{\mu}\boldsymbol{\mu}^T & \boldsymbol{\mu} \\ \boldsymbol{\mu}^T & 1 \end{bmatrix}$. Obviously the mean vector $\boldsymbol{\mu}$ and covariance matrix $\boldsymbol{\Sigma}$ are entangled. The purpose of this layer is to decouple \mathbf{Y} and explicitly write it as the function of input feature matrix \mathbf{X} . We first note that there exists the identity $\boldsymbol{\Sigma} = \frac{1}{N} \mathbf{X}^T \mathbf{X} - \boldsymbol{\mu}\boldsymbol{\mu}^T$. After some elementary manipulations, we have

$$\begin{aligned} \mathbf{Y} &= f_{MPL}(\mathbf{X}) \\ &= \frac{1}{N} \mathbf{A} \mathbf{X}^T \mathbf{X} \mathbf{A}^T + \frac{2}{N} (\mathbf{A} \mathbf{X}^T \mathbf{1} \mathbf{b}^T)_{\text{sym}} + \mathbf{B}, \end{aligned} \quad (18)$$

where $\mathbf{A} = \begin{bmatrix} \mathbf{I} \\ \mathbf{0}^T \end{bmatrix}$ composed of a $d \times d$ identity matrix \mathbf{I} and a d -dimensional zero vector $\mathbf{0}$, \mathbf{b} is a $(d+1)$ -dimensional vector with all elements being zero except the last one which is equal to one, $\mathbf{1}$ is a N -dimensional vector with all elements being one, and $\mathbf{B} = \begin{bmatrix} \mathbf{O} & \mathbf{0} \\ \mathbf{0}^T & 1 \end{bmatrix}$ where \mathbf{O} is a $d \times d$ zero matrix. The notation $(\cdot)_{\text{sym}}$ denotes matrix symmetrization. After such manipulations, the derivative of \mathbf{Y} with respect to \mathbf{X} is straightforward.

TABLE 1
Time (ms) taken by matrix decomposition (single precision arithmetic) of a 256×256 covariance matrix.

Algorithm	CUDA cuSOLVER	Matlab (CPU function)	Matlab (GPU function)
EIG	21.3	1.8	9.8
SVD	52.2	4.1	11.9

Square Root SPD Matrix Layer The purpose of this layer is to compute the square root of SPD matrix \mathbf{Y} , i.e., $\mathbf{Z} = f_{SRML}(\mathbf{Y}) \triangleq \mathbf{Y}^{\frac{1}{2}}$. Similar to matrix power as described previously, the matrix \mathbf{Z} can be computed via EIG or SVD. Specifically, \mathbf{Y} has SVD

$$\mathbf{Y} = \tilde{\mathbf{U}} \tilde{\boldsymbol{\Lambda}} \tilde{\mathbf{U}}^T, \quad (19)$$

where $\tilde{\boldsymbol{\Lambda}} = \text{diag}(\tilde{\lambda}_1, \dots, \tilde{\lambda}_{d+1})$ and $\tilde{\mathbf{U}} = [\tilde{\mathbf{u}}_1 \dots \tilde{\mathbf{u}}_{d+1}]$ are the eigenvalues and eigenvectors of \mathbf{Y} , respectively. The square root of \mathbf{Y} can be computed conveniently as:

$$\mathbf{Z} = f_{SRML}(\mathbf{Y}) = \tilde{\mathbf{U}} \tilde{\boldsymbol{\Lambda}}^{\frac{1}{2}} \tilde{\mathbf{U}}^T, \quad (20)$$

where $\tilde{\boldsymbol{\Lambda}}^{\frac{1}{2}} = \text{diag}(\tilde{\lambda}_1^{\frac{1}{2}}, \dots, \tilde{\lambda}_{d+1}^{\frac{1}{2}})$ is computed as element-wise square root of the eigenvalues. Combining matrix partition layer (18) with square root SPD matrix layer (20), we can accomplish the Gaussian embedding (17).

The backpropagation of our global Gaussian embedding block can be implemented by computing the partial derivative associated with square root SPD matrix layer (20) and matrix partition layer (18), which are denoted by $\frac{\partial l}{\partial \mathbf{Y}}$ and $\frac{\partial l}{\partial \mathbf{X}}$, respectively. Note that derivation of $\frac{\partial l}{\partial \mathbf{Y}}$ shares similar philosophy with that of Eq. (13), and so for simplification we do not repeat here. Given $\frac{\partial l}{\partial \mathbf{Y}}$, we can compute $\frac{\partial l}{\partial \mathbf{X}}$ based on Eq. (18), taking the following form:

$$\frac{\partial l}{\partial \mathbf{X}} = \frac{2}{N} (\mathbf{X} \mathbf{A}^T + \mathbf{1} \mathbf{b}^T) \left(\frac{\partial l}{\partial \mathbf{Y}} \right)_{\text{sym}} \mathbf{A}. \quad (21)$$

The proposed global Gaussian embedding block combines mean vector and covariance matrix. By respecting the Lie group structure of the space of Gaussians, we obtain the square root of an SPD matrix as image representation, which contains both first-order statistics (mean) and second-order statistics (covariance).

3.4 Iterative Matrix Square Root Normalized Covariance Pooling Neural Network

In our MPN-COV-Net and G^2 DeNet, computation of matrix square root heavily depends on EIG or SVD. However, fast implementation of EIG or SVD on GPU is still an open problem. Table 1 presents the running time of EIG and SVD of a 256×256 covariance matrix. Matlab (M) built-in CPU functions delivers over 10x and 5x speedups over its CUDA counterparts and built-in GPU functions, respectively. As such, both our MPN-COV-Net and G^2 DeNet opt for EIG or SVD on CPU for computing matrix square root, greatly restricting the training speed of the networks on GPUs.

To overcome this limitation, we propose a fast training method, called iterative matrix square root normalization of covariance (iSQRT-COV) pooling, depending on

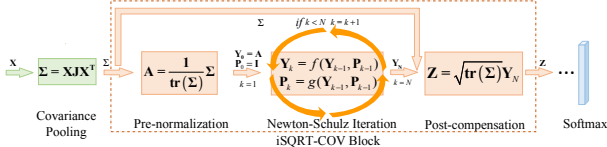


Fig. 4. Diagram of the proposed iSQRT-COV block.

Newton-Schulz iteration [29] in both forward and backward propagations. At the core of iSQRT-COV is a meta-layer with loop-embedded directed graph structure, which consists of three consecutive structured layers, performing pre-normalization, coupled matrix iteration and post-compensation, respectively. The iSQRT-COV block is illustrated in Fig. 4, and the details are described as follows.

Newton-Schulz Iteration Higham [29] studied a class of methods for iteratively computing matrix square root. These methods, termed as Newton-Padé iterations, are developed based on the connection between matrix sign function and matrix square root, together with rational Padé approximation. Specifically, for computing the square root of \mathbf{A} , given $\mathbf{Y}_0 = \mathbf{A}$ and $\mathbf{P}_0 = \mathbf{I}$, for $k = 1, \dots, N$, the coupled iteration takes the following form [29, Chap. 6.7]:

$$\begin{aligned} \mathbf{Y}_k &= \mathbf{Y}_{k-1} p_{lm}(\mathbf{P}_{k-1} \mathbf{Y}_{k-1}) q_{lm}(\mathbf{P}_{k-1} \mathbf{Y}_{k-1})^{-1} \\ \mathbf{P}_k &= p_{lm}(\mathbf{P}_{k-1} \mathbf{Y}_{k-1}) q_{lm}(\mathbf{P}_{k-1} \mathbf{Y}_{k-1})^{-1} \mathbf{P}_{k-1}, \end{aligned} \quad (22)$$

where p_{lm} and q_{lm} are polynomials, and l and m are non-negative integers. According to Eq. (22), \mathbf{Y}_k and \mathbf{P}_k quadratically converge to $\mathbf{A}^{1/2}$ and $\mathbf{A}^{-1/2}$, respectively. However, it converges only locally: if $\|\mathbf{I} - \mathbf{A}\| < 1$ where $\|\cdot\|$ denotes any induced (or consistent) matrix norm. The family of coupled iteration is stable in that small errors in the previous iteration will not be amplified. The case of $l = 0, m = 1$ called *Newton-Schulz iteration* fits for our purpose as no GPU unfriendly matrix inverse is involved:

$$\begin{aligned} \mathbf{Y}_k &= \frac{1}{2} \mathbf{Y}_{k-1} (3\mathbf{I} - \mathbf{P}_{k-1} \mathbf{Y}_{k-1}) \\ \mathbf{P}_k &= \frac{1}{2} (3\mathbf{I} - \mathbf{P}_{k-1} \mathbf{Y}_{k-1}) \mathbf{P}_{k-1}, \end{aligned} \quad (23)$$

where $k = 1, \dots, N$. Clearly Eq. (23) involves only matrix product, suitable for parallel implementation on GPU. Compared to *accurate* square root computed by EIG, one can obtain *approximate* solution with a small number of iterations N , which is determined by cross-validation.

Pre-normalization and Post-compensation As Newton-Schulz iteration only converges locally, we pre-normalize covariance Σ by its trace or Frobenius norm, i.e.,

$$\mathbf{A} = \frac{1}{\text{tr}(\Sigma)} \Sigma \quad \text{or} \quad \frac{1}{\|\Sigma\|_F} \Sigma. \quad (24)$$

Let λ_i be eigenvalues of Σ , arranged in nondecreasing order. As $\text{tr}(\Sigma) = \sum_i \lambda_i$ and $\|\Sigma\|_F = \sqrt{\sum_i \lambda_i^2}$, it is easy to see that $\|\mathbf{I} - \mathbf{A}\|_2$, which equals to the largest singular value of $\mathbf{I} - \mathbf{A}$, is $1 - \frac{\lambda_1}{\sum_i \lambda_i}$ and $1 - \frac{\lambda_1}{\sqrt{\sum_i \lambda_i^2}}$ for the case of trace and Frobenius norm, respectively, both less than 1. Hence, the convergence condition is satisfied.

The above pre-normalization for covariance pooling nontrivially changes the data magnitudes, which produces

side effect on network such that the prevalent ResNet [4] fails to converge. To counteract this adverse influence, after the Newton-Schulz iteration, we accordingly perform post-compensation as follows:

$$\mathbf{Z} = \sqrt{\text{tr}(\Sigma)} \mathbf{Y}_N \quad \text{or} \quad \mathbf{Z} = \sqrt{\|\Sigma\|_F} \mathbf{Y}_N. \quad (25)$$

Alternatively, one may consider Batch Normalization (BN) [56], which does work, successfully helping ResNet convergence. Compared to BN, our post-compensation achieves about 1% higher top-1 accuracy with ResNet-50 architecture on ImageNet (see Section 4.2.1 for details).

To accomplish the backpropagation of our iSQRT-COV block, we derive the gradients associated with the structured layers based on matrix backpropagation methodology [54]. Below we take *pre-normalization by trace* as an example, deriving the corresponding gradients.

BP of Post-compensation Given $\frac{\partial l}{\partial \mathbf{Z}}$ where l is the loss function, the chain rule is of the form $\text{tr}((\frac{\partial l}{\partial \mathbf{Z}})^T d\mathbf{Z}) = \text{tr}((\frac{\partial l}{\partial \mathbf{Y}_N})^T d\mathbf{Y}_N + (\frac{\partial l}{\partial \Sigma})^T d\Sigma)$. After some manipulations, we have

$$\begin{aligned} \frac{\partial l}{\partial \mathbf{Y}_N} &= \sqrt{\text{tr}(\Sigma)} \frac{\partial l}{\partial \mathbf{Z}} \\ \frac{\partial l}{\partial \Sigma} \Big|_{\text{post}} &= \frac{1}{2\sqrt{\text{tr}(\Sigma)}} \text{tr} \left(\left(\frac{\partial l}{\partial \mathbf{Z}} \right)^T \mathbf{Y}_N \right) \mathbf{I}. \end{aligned} \quad (26)$$

BP of Newton-Schulz Iteration Then we will compute the partial derivatives with respect to $\frac{\partial l}{\partial \mathbf{Y}_k}$ and $\frac{\partial l}{\partial \mathbf{P}_k}$, $k = N-1, \dots, 1$, given $\frac{\partial l}{\partial \mathbf{Y}_N}$ obtained by Eq. (26) and $\frac{\partial l}{\partial \mathbf{P}_N} = 0$. As the matrix Σ is symmetric, it is easy to see from Eq. (23) that \mathbf{Y}_k and \mathbf{P}_k are both symmetric. According to the chain rules (omitted hereafter for simplicity) of matrix backpropagation and after some manipulations, for $k = N, \dots, 2$, we can derive

$$\begin{aligned} \frac{\partial l}{\partial \mathbf{Y}_{k-1}} &= \frac{1}{2} \left(\frac{\partial l}{\partial \mathbf{Y}_k} (3\mathbf{I} - \mathbf{Y}_{k-1} \mathbf{P}_{k-1}) - \mathbf{P}_{k-1} \frac{\partial l}{\partial \mathbf{P}_k} \mathbf{P}_{k-1} \right. \\ &\quad \left. - \mathbf{P}_{k-1} \mathbf{Y}_{k-1} \frac{\partial l}{\partial \mathbf{Y}_k} \right) \\ \frac{\partial l}{\partial \mathbf{P}_{k-1}} &= \frac{1}{2} \left((3\mathbf{I} - \mathbf{Y}_{k-1} \mathbf{P}_{k-1}) \frac{\partial l}{\partial \mathbf{P}_k} - \mathbf{Y}_{k-1} \frac{\partial l}{\partial \mathbf{Y}_k} \mathbf{Y}_{k-1} \right. \\ &\quad \left. - \frac{\partial l}{\partial \mathbf{P}_k} \mathbf{P}_{k-1} \mathbf{Y}_{k-1} \right). \end{aligned} \quad (27)$$

The final step of this layer is concerned with the partial derivative with respect to $\frac{\partial l}{\partial \mathbf{A}}$, which is given by

$$\frac{\partial l}{\partial \mathbf{A}} = \frac{1}{2} \left(\frac{\partial l}{\partial \mathbf{Y}_1} (3\mathbf{I} - \mathbf{A}) - \frac{\partial l}{\partial \mathbf{P}_1} - \mathbf{A} \frac{\partial l}{\partial \mathbf{Y}_1} \right). \quad (28)$$

BP of Pre-normalization Note that here we need to combine the gradient of the loss function l with respect to Σ , backpropagated from the post-compensation layer. As such, by referring to Eq. (24), we make similar derivations as before and obtain

$$\begin{aligned} \frac{\partial l}{\partial \Sigma} &= -\frac{1}{(\text{tr}(\Sigma))^2} \text{tr} \left(\left(\frac{\partial l}{\partial \mathbf{A}} \right)^T \Sigma \right) \mathbf{I} + \frac{1}{\text{tr}(\Sigma)} \frac{\partial l}{\partial \mathbf{A}} \\ &\quad + \frac{\partial l}{\partial \Sigma} \Big|_{\text{post}}. \end{aligned} \quad (29)$$

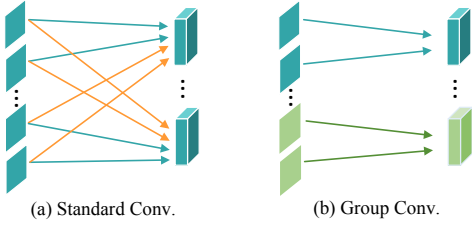


Fig. 5. Comparison of (a) Standard convolution (Conv.) and (b) Group convolution.

If we adopt *pre-normalization by Frobenius norm*, the gradients associated with post-compensation become

$$\begin{aligned} \frac{\partial l}{\partial \mathbf{Y}_N} &= \sqrt{\|\Sigma\|_F} \frac{\partial l}{\partial \mathbf{Z}} \\ \frac{\partial l}{\partial \Sigma} \Big|_{\text{post}} &= \frac{1}{2\|\Sigma\|_F^{3/2}} \text{tr} \left(\left(\frac{\partial l}{\partial \mathbf{Z}} \right)^T \mathbf{Y}_N \right) \Sigma, \end{aligned} \quad (30)$$

and that with respect to pre-normalization is

$$\begin{aligned} \frac{\partial l}{\partial \Sigma} &= -\frac{1}{\|\Sigma\|_F^3} \text{tr} \left(\left(\frac{\partial l}{\partial \mathbf{A}} \right)^T \Sigma \right) \Sigma + \frac{1}{\|\Sigma\|_F} \frac{\partial l}{\partial \mathbf{A}} \\ &\quad + \frac{\partial l}{\partial \Sigma} \Big|_{\text{post}}, \end{aligned} \quad (31)$$

while the backward gradients of Newton-Schulz iteration (27) keep unchanged. Finally, given $\frac{\partial l}{\partial \Sigma}$, one can derive the gradient of the loss function l with respect to input feature matrix \mathbf{X} , which shares the same form with Eq. (14).

3.5 Compactness of Covariance Representation

Given an input feature matrix $\mathbf{X} \in \mathbb{R}^{d \times M}$ consisting of M samples with d -dimension, size of covariance representation is $d \times (d+1)/2$ after matrix vectorization by considering the symmetry. Taking $d = 512$ or $d = 1024$ as an example, the size of covariance representation is 131,328 or 524,800. Such high dimensional representation inevitably leads to a huge number of parameters, bringing unfordable computation and memory costs. To deal with this problem, we propose two strategies for dimensionality reduction (DR), i.e., progressive 1×1 convolutions for DR of input features and group convolution [30] for DR of covariance matrix.

Since the dimension of input features decides size of covariance representation, we first introduce a strategy of progressive 1×1 convolutions to reduce the dimension of input features. The 1×1 convolution is first introduced in [57], and has been widely used in deep CNN architectures [3], [4], [5] for parameter reduction. However, an abrupt dimensionality reduction (e.g., directly from 2080 to 128) may hurt the performance of covariance representations. Therefore, we propose to progressively reduce the dimension of input features from d to \hat{d} ($\hat{d} \ll d$) using a set of consecutive 1×1 convolutions, i.e., $d = d_0 \rightarrow d_1 \rightarrow \dots \rightarrow d_K = \hat{d}$ with $d_{k-1} > d_k$. In this way, dimension of covariance representation can be effectively reduced to $\hat{d} \times (\hat{d} + 1)/2$ (e.g., 8256 for $\hat{d} = 128$). Compared with dimensionality reduction using only one 1×1 convolution, our progressive convolutions can achieve better performance.

Once dimension of input is determined, we can further reduce the size of covariance representation by learning

a low-dimensional linear transform matrix \mathbf{W} on covariance representation \mathbf{z} , which corresponds to inserting a FC layer ($\hat{\mathbf{z}} = \mathbf{W}\mathbf{z} + \mathbf{b}$) after covariance pooling. The number of parameters of \mathbf{W} is $d_z \times d_{\hat{z}}$, where d_z and $d_{\hat{z}}$ are dimensions of \mathbf{z} and $\hat{\mathbf{z}}$, respectively. If d_z is very high, transform matrix \mathbf{W} will involve of many parameters, increasing computation and memory costs. Therefore, we introduce group convolution [30] to alleviate this problem. As shown in Fig. 5, different from standard convolution, group convolution divides \mathbf{z} into G groups and performs convolution operation in each sub-group. As such, number of parameters of \mathbf{W} can be decreased to $(d_z \times d_{\hat{z}})/G$, very suitable for high dimensional covariances.

4 EXPERIMENTS

To evaluate the representation and generalization abilities of the proposed methods, we conduct experiments on both large-scale object classification and scene categorization, small-scale fine-grained visual recognition and texture classification as well as large-scale species classification competition. We first describe implementation details of our methods. Then we make ablation study of the proposed methods on large-scale ImageNet dataset, and compare with state-of-the-art methods on ImageNet [33] and Place365 [34]. Additionally, we verify the generalization ability of the proposed methods through transferring them to three fine-grained (i.e., Birds-CUB200-2011 [35], Aircrafts [36] and Cars [37]) and two texture image datasets (i.e., Indoor67 [39] and DTD [38]). Finally, we show the results on iNaturalist Challenge 2018 held in CVPR 2018 workshop on FGVC5.

4.1 Implementation Details

To implement MPN-COV block, we use the EIG algorithm on CPU in single-precision floating-point format, as the EIG algorithm on GPU is much slower, despite the overhead due to data transfer between GPU memory and CPU memory. Since MPN-COV allows non-negative eigenvalues, we truncate to zeros the eigenvalues smaller than $\text{eps}(\lambda_1)$, which is a matlab function denoting the positive distance from the largest eigenvalue λ_1 to its next larger floating-point number. For achieving the global Gaussian embedding block, as suggested in [18], we use SVD to compute square root SPD matrix because SVD is numerically more stable, and SVD algorithm is implemented on CPU as well. Meanwhile, we add a small positive number 1e-3 to the diagonal entries of Gaussian embedded matrices for numerical stability. The implementation of iSQRT-COV block is encapsulated in three computational modules, which accomplish forward&backward computation of pre-normalization layer, Newton-Schulz iteration layer and post-compensation layer, respectively. We implement above methods based on the MatConvNet package [32]; iSQRT-COV-Net is also implemented using Pytorch.

The proposed GCP blocks are inserted after the last convolution layer (with ReLU) of deep CNNs. Unless otherwise stated, we discard the last downsampling operation so that we can have larger number of features, and add one 1×1 convolution with $d = 256$ channels before our

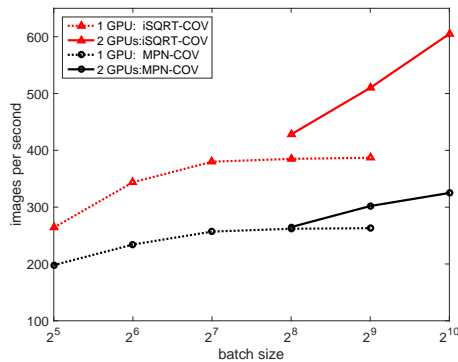
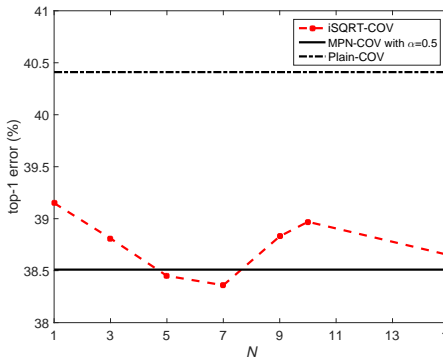
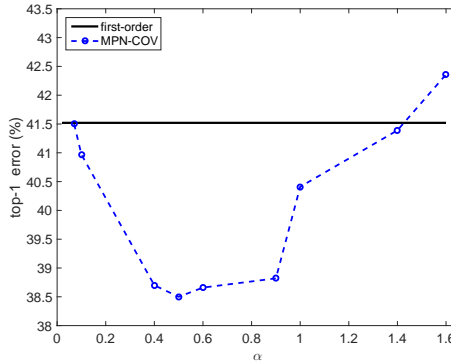


Fig. 6. Effect of α on MPN-COV with AlexNet. Fig. 7. Impact of number N of Newton-Schulz iterations on iSQRT-COV with AlexNet on Ima-geNet. Top-1 errors (1-crop) are reported. The bold line indicates the result of original AlexNet.

covariance pooling for all CNN architectures but AlexNet. As such, the last convolution layer outputs $c \times c \times 256$ feature maps, where c is the height/width of feature maps, resulting in a 256×256 covariance matrix (also $32,896\text{-}d$ covariance representation after matrix vectorization). We train our networks using mini-batch stochastic gradient descent algorithm with a momentum of 0.9 and a weight decay of 5×10^{-4} . All programs run on two PCs each of which is equipped with a 4-core Intel i7-4790k@4.0GHz CPU, 32G RAM, 512GB Samsung PRO SSD and two Titan Xp GPUs. The remaining hyper-parameters of training networks will be described where appropriate in following subsections.

4.2 Large-scale Object Classification on ImageNet

4.2.1 Ablation Study

We first analyze the proposed methods on large-scale ImageNet dataset, which contains 1.28M training images, 50K validation images and 100K testing images collected from 1K classes. On this dataset, we follow [2] for data augmentation, and adopt the commonly used 1-crop or 10-crop prediction for performance evaluation. Following the common settings [1], [2], [4], we report the results on the validation set. Specifically, we study the effect of parameter α on MPN-COV and compare various normalization methods on GCP, impacts of number N of Newton-Schulz iterations and post-compensation on iSQRT-COV, speedup ratio of training iSQRT-COV-Net over MPN-COV-Net, and effect of compactness of covariance representations.

MPN-COV: Effect of parameter α Our MPN-COV has a key parameter α , and we evaluate it under AlexNet architecture. Our MPN-COV-Net is trained up to 20 epochs, where the learning rates follow exponential decay, changing from $10^{-1.2}$ to 10^{-5} with a batch size of 128. Fig. 6 shows top-1 error vs. α using single-crop prediction. We first note that the Plain-COV ($\alpha = 1$, no normalization) produces an error rate of 40.41%, about 1.1% less than the original AlexNet. When $\alpha < 1$, the normalization function shrinks eigenvalues larger than 1.0 and stretches those less than 1.0. As α (less than 1.0) decreases, the error rate continuously gets smaller until the smallest value at around $\alpha = \frac{1}{2}$. With further decline of α , however, we observe the error rate grows consistently and soon is larger than that of the Plain-COV. Note that over the interval $[0.4, 0.9]$ the performance

TABLE 2
Top-1 error (% , 1-crop) of GCP with various normalization methods under AlexNet architecture.

method	MPN (ours)	M-Fro	M- ℓ_2	E-PN [17]	top-1 Err.
Baseline	—	—	—	—	41.52
GCP	×	×	×	×	40.41
	✓	×	×	×	38.51
	✓	✓	×	×	39.93
	✓	×	✓	×	39.62
	✓	×	×	✓	40.75
	×	✓	×	×	39.87
	×	×	✓	×	39.65
	×	×	×	✓	39.89

of MPN-COV varies insignificantly. When $\alpha > 1$, the effect of normalization is contrary, i.e., eigenvalues less than 1.0 are shrunk while those larger than 1.0 are stretched, which is not beneficial for covariance representations as indicated by the consistent growth of the error rates. As such, we set $\alpha = \frac{1}{2}$ throughout the following experiments.

MPN-COV: Comparison of various normalization methods We compare four kinds of normalization methods, i.e., MPN, M-Fro, M- ℓ_2 and element-wise power normalization (E-PN) followed by ℓ_2 -normalization [17]. Table 2 summarizes the comparison results, where we can see that all GCP methods outperform the original network, and all normalization methods improve over the plain COV; among them, our MPN obtains the best result, and outperforms M-Fro, M- ℓ_2 and E-PN by $\sim 1.3\%$, $\sim 1.1\%$ and $\sim 1.3\%$, respectively. Note that GCP with MPN (i.e., MPN-COV) followed by further normalization, either by M-Fro, M- ℓ_2 or E-PN, produces negative gains, so we do not perform any further normalization on our MPN-COV in following experiments.

iSQRT-COV: Number N of Newton-Schulz iterations Here we assess impact of N by employing AlexNet as a backbone model, and using the same hyper-parameters as MPN-COV except the initial learning rate, which is set to $10^{-1.1}$. The top-1 error rate (in 1-crop prediction) vs. N is illustrated in Fig. 7. With single one iteration, our iSQRT-COV outperforms Plain-COV by 1.3%. As iteration number grows, the error rate of iSQRT-COV gradually declines. With 3 iterations, iSQRT-COV is comparable to MPN-COV, having only 0.3% higher error rate, while performing marginally better than MPN-COV between 5 and 7

TABLE 3
Impact of post-compensation on iSQR-COV with ResNet-50 architecture on ImageNet.

Pre-normalization	Post-compensation	Top-1 Err.	Top-5 Err.
Trace	w/o	N/A	N/A
	w/ BN [56]	23.12	6.60
	w/ Trace	22.14	6.22

iterations. The results after $N = 7$ show growth of iteration number is not helpful for improving accuracy. As larger N incurs higher computational cost, we set N to 5 in the remaining experiments for balancing efficiency and accuracy. An interesting phenomenon is that approximate square root normalization in iSQR-COV achieves a little gain over the exact one obtained via EIG, which may suggest the fact that matrix square root is not the optimal normalization method for covariance pooling, encouraging development of better normalization methods in the future work.

iSQR-COV: Significance of post-compensation As discussed in Section 3.4, post-compensation in iSQR-COV helps to eliminate the side effect resulting from pre-normalization. We verify its significance with ResNet-50 architecture. Table 3 summarizes impact of different schemes on iSQR-COV-Net, including simply do nothing (i.e., without post-compensation), Batch Normalization (BN) [56] and our post-compensation scheme. We note that iSQR-COV-Net fails to converge without post-compensation. Careful observations show that in this case the gradients are very small (on the order of 10^{-5}), and larger learning rate helps little. Option of BN helps the network converge, but producing about 1% higher top-1 error rate than our post-compensation scheme. The comparison above suggests that our post-compensation is essential for achieving state-of-the-art results with deep CNN architectures, e.g., ResNet-50.

MPN-COV VS. iSQR-COV in training speed To show acceleration effect of iSQR-COV, we compare in Fig. 8 training speed between MPN-COV-Net and iSQR-COV-Net with both 1-GPU and 2-GPU configurations. For 1-GPU configuration, the speed gap vs. batch size between the two methods keeps nearly constant. For 2-GPU configuration, their speed gap becomes more significant when batch size gets larger. As can be seen, the speed of iSQR-COV-Net continuously grows with increase of batch size while MPN-COV-Net tends to saturate when batch size is larger than 512. Clearly, by avoiding GPU unfriendly EIG or SVD, iSQR-COV can speed up MPN-COV and make better use of computing power of multiple GPUs.

Compactness of covariance representations In default setting, our methods output a 32k-dimensional covariance representation. In this paper, the strategies of progressive 1×1 convolutions and group convolution [30] are proposed to further compact covariance representations. We evaluate them using iSQR-COV with ResNet-50 architecture. Table 4 summarizes the results of our iSQR-COV with various compactness settings and additional parameters (Params.) brought by dimensionality reduction (DR), where we use a single 1×1 convolution to decrease dimension of convolution features from 2048 to 256, 128 and 64. Then, progressive DR are performed based on two consecutive 1×1 convolutions, i.e., $2048 \rightarrow 512 \rightarrow 256$, $2048 \rightarrow 512 \rightarrow 128$ and

TABLE 4
Error rate (%) of compacting covariance representation (Repr.) with ResNet-50 on ImageNet. FC indicates number of parameters in final FC layer.

Method	DR	Repr.	Top-1/Top-5	Params.	FC
GAP [4]	N/A	2K	24.7/7.8	N/A	2M
iSQR-COV	$2048 \rightarrow 256$	32K	22.14/6.22	0.53M	32M
	$2048 \xrightarrow{512} 256$	32K	21.72/5.99	1.13M	32M
	$2048 \rightarrow 128$	8K	22.78/6.43	0.26M	8M
	$2048 \xrightarrow{512} 128$	8K	22.33/6.28	1.07M	8M
	$2048 \rightarrow 64$	2K	23.73/6.99	0.13M	2M
	$2048 \xrightarrow{256} 64$	2K	22.98/6.61	0.54M	2M
	4th row & 1G	2K	22.40/6.35	18.9M	2M
	4th row & 2G	2K	22.84/6.60	9.6M	2M
	4th row & 4G	2K	23.11/6.77	4.3M	2M

TABLE 5
Error rate (%) and time of FP+BP (ms) per image of different covariance pooling methods with AlexNet on ImageNet. Numbers in parentheses indicate FP time. *Following [26], improved B-CNN successively performs matrix square root, element-wise square root and ℓ_2 normalizations.

Method	Top-1 Err.	Top-5 Err.	Time
AlexNet [1]	41.8	19.2	1.32 (0.77)
B-CNN [19]	39.89	18.32	1.92 (0.83)
DeepO ₂ P [18]	42.16	19.62	11.23 (7.04)
Improved B-CNN* [26]	40.75	18.91	15.48 (13.04)
MPN-COV-Net	38.51	17.60	3.89 (2.59)
G ² DeNet	38.48	17.59	9.86 (5.88)
iSQR-COV-Net(Frob.)	38.78	17.67	2.56 (0.81)
iSQR-COV-Net(trace)	38.45	17.52	2.55 (0.81)

$2048 \rightarrow 256 \rightarrow 64$. We do not employ more 1×1 convolutions as they will bring additional parameters. Meanwhile, size of covariance representation with $2048 \rightarrow 512 \rightarrow 128$ (4th row) are further reduced to 2K using group convolutions of one group, two and four groups, which are indicated by 1G, 2G and 4G, respectively.

As listed in Table 4, by using a single 1×1 convolution, the recognition error increases about 1.0% and 1.6% when d decreases from 256 to 128 and 64, respectively. The results of progressive DR versions are better than their counterparts based on a single 1×1 convolution, showing the strategy of progressive DR is helpful to preserve classification accuracy for low-dimensional representations. Combining progressive 1×1 convolutions with group convolution, we can obtain 22.4% top-1 error with 2K-dimensional representations, still clearly outperforming the original ResNet-50 with first-order GAP. Above results verify the effectiveness of our compactness covariance representations. Our compactness strategies can obtain effective low-dimensional representations, very suitable for large scale species classification problem, which will be shown in Section 4.6.

4.2.2 Comparisons with Different Methods

Comparison with other deep global GCP methods We compare different variants of MPN-COV with existing deep global GCP methods using AlexNet architecture, including B-CNN [19], DeepO₂P [18] and improved B-CNN [26]. All methods are trained from scratch on ImageNet. We implement B-CNN, DeepO₂P and improved B-CNN using public available source code released by the respective authors, and try our best to tune hyper-parameters for them. Note

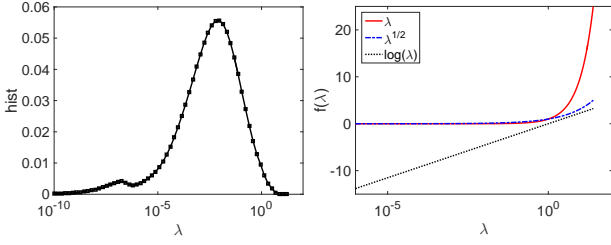


Fig. 9. Illustration of empirical distribution of eigenvalues (left) and normalization functions (right).

TABLE 6

Error (% in 1-crop) comparison with local second-order networks under ResNet-50 and deep CNN architectures on ImageNet.

Method	Backbone model	Top-1 Err.	Top-5 Err.
ResNet-50 [4]	ResNet-50	24.7	7.8
FBN [46]		24.0	7.1
SORT [47]		23.82	6.72
SE-Net [58]		23.29	6.62
CBAM [59]		22.66	6.31
MPN-COV-Net		22.73	6.54
iSQRT-COV-Net		22.14	6.22
ResNet-101 [4]	ResNet-101	23.6	7.1
SE-Net [58]		22.38	6.07
CBAM [59]		21.51	5.69
iSQRT-COV-Net		21.21	5.68
ResNet-152 [4]	ResNet-152	23.0	6.7
DenseNet-201 [5]	DenseNet-201	22.58	6.34
iSQRT-COV-Net		20.69	5.48

that we use the suggested implementation of improved B-CNN in [26], i.e., FP by SVD and BP by Lyapunov equation. The results of different methods are listed in Table 5. We can see that our MPN-COV-Net, G²DeNet and iSQRT-COV-Net obtain similar results, and clearly outperform B-CNN, DeepO₂P and improved B-CNN. We owe the gains to matrix power normalization, benefiting robust covariance estimation and proper usage of geometry. The improved B-CNN achieves an unsatisfactory result, which can be regraded as performing element-wise power normalization followed by ℓ_2 normalization behind our MPN-COV. This result suggests that further normalization hurts MPN-COV on large-scale ImageNet classification, which is consistent with the observation in Table 2. Additionally, for iSQRT-COV-Net, pre-normalization by trace performs better than Frobenius norm. G²DeNet achieves similar results with MPN-COV-Net, suggesting that combination of mean vector brings trivial gains, and so we just report the results of MPN-COV-Net and iSQRT-COV-Net (trace) in following comparisons.

Why LERM does not work well? DeepO₂P exploits matrix logarithm normalization (i.e., LERM [12]) to exploit geometry of covariance, and we claim it is not suit for deep CNNs. Firstly, the Pow-E metric in MPN-COV improves numerical stability of covariance matrices over LERM. The LERM requires the eigenvalues involved to be *strictly positive* [12] while the Pow-E metric allows *non-negative* eigenvalues [25]. For LERM the common method is to add a small positive number ϵ to eigenvalues for numerical stability. Although ϵ can be decided by cross-validation, it is difficult to seek the optimal ϵ suitable for training of deep CNN. For example, [18] suggest $\epsilon = 10^{-3}$, which will smooth out eigenvalues less than 10^{-3} . In contrast, the Pow-

E metric do not need such a remedy. Furthermore, from the distribution perspective, the matrix logarithm reverses the order of the significance of eigenvalues, harmful for covariance representations. To make a qualitative analysis, we randomly select 300,000 images from training set of ImageNet, and estimate per-image sample covariances using the outputs of the last convolution layer in AlexNet model. Then, we compute eigenvalues of all covariances using EIG in single-precision floating-point format. The histogram of eigenvalues is shown in Fig. 9 (left), where zero eigenvalues are excluded for better view. Fig. 9 (right) shows the two normalization functions over $[10^{-5}, 10]$. We can see $\log(\lambda)$ considerably changes the eigenvalue magnitudes, reversing the order of significance of eigenvalues, e.g., a significant eigenvalue $\lambda = 50 \mapsto \log(\lambda) \approx 3.9$ but an insignificant one $\lambda = 10^{-3} \mapsto \log(\lambda) \approx -6.9$. Since significant eigenvalues are generally more important in that they capture the statistics of principal directions along which the feature variances are larger, matrix logarithm will harm covariance pooling.

Comparison with deep local second-order networks

In Table 6, we compare our MPN-COV-Net and iSQRT-COV-Net, using ResNet-50 architecture, with deep local second-order networks [46], [47]. Clearly, the two networks integrating local second-order statistics improve over the original one. Our MPN-COV-Net and iSQRT-COV-Net employing matrix square root normalization, are superior to FBN [46] and SORT [47]. These results demonstrate again the effectiveness of our MPN-COV. Similar to the results with AlexNet, iSQRT-COV-Net outperforms MPN-COV-Net by 0.6% in top-1 error.

Comparison with various CNN architectures

In the end of this subsection, we evaluate our MPN-COV with different CNN architectures. Since we modify the existing CNN architectures (as described in Section 4.1), we first compare our MPN-COV with the modified CNN architectures. Fig. 10(a) illustrates the results of different networks with 1-crop prediction, from it we can see that our MPN-COV outperforms consistently the corresponding modified CNN architectures by a clear margin. Then, we combine the proposed MPN-COV with five deep CNN models, including AlexNet [1], VGG-M [60], VGG-VD16 [2], ResNet-50 [4] and ResNet-101 [4]. Here we compare with the resulted MPN-COV-Net with the original CNN models and the networks with similar architectures. The top-1 error and top-5 error of different networks with 10-crop prediction are given in Fig. 10(b) and Fig. 10(c), respectively. The results of compared methods are duplicated from the original papers.

Using AlexNet as backbone model, we compare MPN-COV-Net with the original AlexNet and VGG-F [60]. Our MPN-COV-Net performs much better than both of them. Comparing MPN-COV-Net using VGG-M [60] with the original one, Zeiler & Fergus [61] and OverFeat [62], our MPN-COV-Net shows much better performance than them. Using VGG-VD16 as backbone model, our MPN-COV-Net outperforms the original VGG-VD16 [2] by $\sim 2.7\%$ in terms of top-1 error, and performs better than GoogleNet [3] and PReLU-net B [63] by $\sim 1.4\%$ and $\sim 0.4\%$ in terms of top-5 error, respectively. For ResNet-50 and ResNet-101 architectures, the results show that our MPN-COV-Net performs 1.65% and 2.04% better than the original ones in terms of top-1 error, respectively. Noted that our MPN-COV with

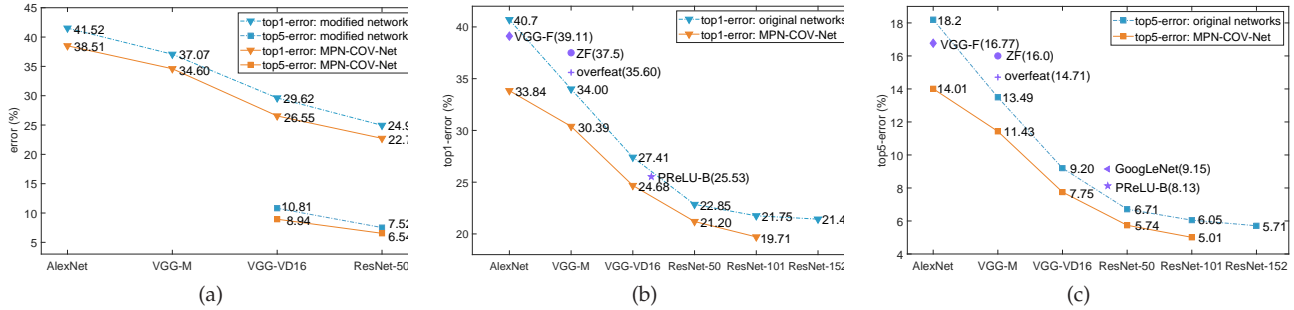


Fig. 10. Classification error comparison with different CNN architectures. (a) shows MPN-COV-Net vs. corresponding modified first-order networks in Top-1/Top-5 errors (1-crop prediction). (b) and (c) show MPN-COV-Net vs. original first-order networks and similar CNN architectures in Top-1 error and Top-5 error (10-crop prediction), respectively.

TABLE 7
Comparison of classification error (%) with 10-crop prediction on Places365 dataset.

	VGG-VD16 [2]	GoogLeNet [3]	ResNet-50 [4]	ResNet-152 [34]	B-CNN (ResNet-50)	iSQRT-COV-Net (ResNet-50)
Top-1 Error	44.76	46.37	44.82	45.26	44.24	43.68
Top-5 Error	15.09	16.12	14.71	14.92	14.27	13.73

ResNet-50 and ResNet-101 outperform the original ResNet-101 and ResNet-152 based on first-order GAP, respectively. We also compare iSQRT-COV-Net, in Table 6, with the recently proposed SE-Net [58], CBAM [59] using ResNet-50 and ResNet-101 in 1-crop prediction. Our iSQRT-COV-Net consistently improves SE-Net and CBAM. Compared with DenseNet-201 [5], our iSQRT-COV-Net obtains $\sim 1.9\%$ gains in top-1 error. Above results show our GCP methods can effectively improve CNNs with various architectures.

4.3 Large-scale Scene Categorization on Place365

We evaluate our methods on large-scale scene categorization using Places365 dataset [34], which contains about 1.8 million training images and 36,500 validation images collected from 365 scene categories. Following the common settings in [34], we resize all images to 256×256 and randomly crop a 224×224 image patch or its flip for training. The inference is performed with 10-crop prediction, and we report the results on validation set for comparison. Here we compare our iSQRT-COV-Net, using ResNet-50, with five kinds of CNN models, i.e., GoogLeNet [3], VGG-VD16 [2], ResNet-50 [4], ResNet-152 [4] and B-CNN with ResNet-50. The results of different methods are given in Table 7, from it we can see that our iSQRT-COV-Net achieves the best results, and outperforms the original ResNet-50 by about 1.2% and 1% in Top-1 and Top-5 errors, respectively. Meanwhile, iSQRT-COV-Net is superior to B-CNN under the same settings. The results on both ImageNet and Place365 verify our proposed methods can significantly improve the representation ability of deep CNNs, achieving higher classification accuracy.

4.4 Fine-grained Visual Recognition

To assess the generalization ability of the proposed methods, we transfer our networks pre-trained on ImageNet to fine-grained visual recognition. The experiments are conducted on three benchmarks. Among them, *Birds-200-2011* [35] is a challenging dataset, including 11,788 images from 200 bird species. *FGVC-aircraft* [36] is a part of the FGComp 2013

TABLE 8
Comparison of accuracy (%) on fine-grained benchmarks.

	Method	Birds	Aircrafts	Cars
VGG-D16	VGG-VD16 [19]	70.4	76.6	79.8
	NetVLAD [48]	81.9	81.8	88.6
	NetFV [64]	79.9	79.0	86.2
	B-CNN [19]	84.0	83.9	90.6
	CBP [40]	84.3	84.1	91.2
	LRBP [41]	84.2	87.3	90.9
	KP [43]	86.2	86.9	92.4
	HIHCA [44]	85.3	88.3	91.7
	Improved B-CNN [26]	85.8	88.5	92.0
	MPN-COV (Ours)	86.7	89.9	92.2
ResNet-50	G ² DeNet (Ours)	87.1	89.0	92.5
	iSQRT-COV (Ours)	87.2	90.0	92.5
	ResNet-50 [43]	78.4	79.2	84.7
	CBP [40]	81.6	81.6	88.6
	KP [43]	84.7	85.7	91.1
	iSQRT-COV 8K (Ours)	87.3	89.5	91.7
iSQRT-COV 32K (Ours)	88.1	90.0	92.8	
iSQRT-COV with ResNet-101 (Ours)	88.7	91.4	93.3	

challenge, which consists of 10,000 images across 100 aircraft classes. *FGVC-Cars* [37] is also presented as a part of the FGComp 2013 challenge, containing 16,185 images from 196 car categories. We employ the fixed training/testing splits provided by the dataset developers, and train or evaluate our networks using neither part annotations nor bounding boxes. For fair comparison, we follow [19] for experimental setting and evaluation protocol. Specifically, we resize the shorter side of input images to 448, and crop center 448×448 patches. We replace 1000-way softmax layer of our pre-trained networks by a k -way softmax layer, where k is number of classes in the corresponding fine-grained dataset, and fine-tune the networks for 50~100 epochs with a small learning rate lr (e.g., $10^{-2.1}$) for all layers except the last FC layer, which is set to $5 \times lr$. The random horizontal flipping is used for data augmentation. After fine-tuning, we perform ℓ_2 -normalization on the outputs of our GCP blocks, and feed them to train k one-vs-all linear SVMs with parameter $C = 1$. We predict the label of a test image by averaging

TABLE 9
Classification accuracy (in %) of different methods on DTD and Indoor67.

Method	Backbone Model	DTD	Indoor67
VGG-VD16 [42]	VGG-VD16	62.9±0.8	67.6
B-CNN [19]	VGG-VD16	72.9±0.8	79.0
FASON [42]	VGG-VD16	72.9±0.7	80.8
Deep-TEN [65]	ResNet-50	N/A	76.2
MFAFV-Net [51]	VGG-VD16	N/A	81.1
iSQRT-COV-Net	VGG-VD16	74.0±0.8	81.4
	ResNet-50	74.8±1.0	83.5

SVM scores of the image and its horizontal flip.

Table 8 presents classification results of different methods, where our networks significantly improve the original networks under either VGG-VD16 or ResNet-50. When VGG-VD16 is used as backbone model, our proposed methods are superior to both deep CNNs with trainable BoVW (i.e., NetVLAD [48] and NetFV [64]) and deep CNNs with global approximate high-order pooling (i.e., CBP [40], LRBP [41], KP [43] and HIHCA [44]) by a clear margin. Additionally, our MPN-COV and its variants also outperform other deep GCP methods, i.e., B-CNN [19] and improved B-CNN [26]. With ResNet-50 architecture, iSQRT-COV (8K) respectively outperforms KP by about 2.6%, 3.8% and 0.6% on Birds, Aircrafts and Cars, and iSQRT-COV (32K) further improves accuracy. On all fine-grained datasets, existing methods employing 50-layer ResNet are no better than their counterparts with 16-layer VGG-VD. The reason may be that the last convolution layer of pre-trained ResNet-50 outputs 2048-dimensional features, much higher than 512-dimensional one of VGG-VD, which are not suitable for existing second- or higher-order pooling methods. *Different from all existing methods, our methods perform dimensionality reduction and deem second-order pooling as a component of CNN models, pre-trained on large-scale datasets.* Using pre-trained iSQRT-COV-Net with ResNet-101, we establish state-of-the-art results on three fine-grained benchmarks.

4.5 Texture Classification

We also transfer our iSQRT-COV-Net to texture classification, where DTD [38] and Indoor67 [39] are employed. *Indoor67* has 6,700 images from 67 indoor scene categories, where 80 and 20 images per-category are used for training and test, respectively. *DTD* consists of 5,640 material images collected from 47 classes, and pre-defined splits in [38] are used for evaluation. We adopt the same experimental settings with [19] for fair comparison. The results of different methods are listed in Table 9, where our iSQRT-COV-Net with VGG-VD16 architecture performs much better than the original model and clearly outperforms other deep second-order pooling networks, i.e., B-CNN [19] and FASON [42]. Meanwhile, our iSQRT-COV-Net is superior to Deep-TEN [65] and MFAFV-Net [51] (i.e., deep BoVW methods) using ResNet-50 and VGG-VD16 as backbone models, respectively. The results on both FGVC and texture classification demonstrate our GCP methods can significantly improve the generalization ability of deep CNNs.

TABLE 10
Top-3 error (in %) of different methods on iNaturalist Challenge 2018.

Method	Description	Top-3 Err.
ResNet-152	320×320 input	16.623
	392×392 input	16.024
iSQRT-COV-Net	320×320 input	15.038
	392×392 input	14.625
Our Fusion I	3 × ResNet-152 Model	14.625
Our Fusion II	3 × iSQRT-COV-Net Model	13.409
Our Fusion III	Fusion I + Fusion II	13.068
Runner-up	Deep Learning Analytics	14.214

4.6 iNaturalist Challenge 2018

As part of the FGVC5 workshop at CVPR 2018, iNaturalist Challenge 2018 is a large-scale species classification competition, which contains over 8,000 species with 437,513 training, 24,426 validation and 149,394 test images. This dataset suffers from many visually similar species and high class imbalance, which are extremely difficult for accurate classification without expert knowledge. We use ResNet-152 pre-trained on ImageNet-11K as backbone model, and perform fine-tuning on training and validation sets. The top-3 error is reported on test server for comparison. To efficiently classify a large number of species, we use fast MPN-COV (i.e., iSQRT-COV with 3 iterations), and use a 1×1 convolution with 160 channels before GCP, leading to $\sim 12K$ dimensional representations, connected to 8142-way softmax classifier. Table 10 gives the results of compared methods, where iSQRT-COV-Net distinctly outperforms the original ResNet-152 in configurations of both different input image sizes and ensemble models. By fusing iSQRT-COV-Net and ResNet-152 models, we positioned the first place, and outperforms the runner-up by $\sim 1.2\%$. Note that only ensemble of iSQRT-COV-Net models is still better than the runner-up by $\sim 0.8\%$, showing effectiveness of our method.

5 CONCLUSION

This paper proposed a global matrix power normalized covariance pooling (MPN-COV) method and its variants to summarize the outputs of the last convolution layer for final prediction, aiming at improving the representation and generalization abilities of deep CNNs. We disclosed the mechanisms underlying MPN-COV from the perspectives of robust statistical modeling and Riemannian geometry. Starting from MPN-COV, we proposed a global Gaussian embedding method (i.e., G^2 DeNet), an iterative matrix square root normalization method (i.e., iSQRT-COV) and dimensionality reduction strategies for combining additional first-order information, speeding up training of MPN-COV and compacting covariance representations, respectively. These methods further enhance practicability of our MPN-COV. The comprehensive experiments on both large-scale and small-scale benchmarks verified our MPN-COV and its variants achieve a clear performance boost with diversified deep CNN architectures, achieving state-of-the-art classification accuracy. In view of the effectiveness and architecture-independence of the proposed methods, they have the potential to be a commodity component in the existing deep CNN models, and can motivate interests in future exploration of higher-order information in design

of novel CNN architectures. In future, we will apply the proposed MPN-COV methods to other vision tasks, such as object detection [66] and semantic segmentation [67].

ACKNOWLEDGMENTS

The work was supported by the National Natural Science Foundation of China (Grant No. 61471082, 61671182 and 61806140). Qilong Wang was supported by China Post-doctoral Programme Foundation for Innovative Talent.

REFERENCES

- [1] A. Krizhevsky, I. Sutskever, and G. E. Hinton, "ImageNet classification with deep convolutional neural networks," in *NIPS*, 2012.
- [2] K. Simonyan and A. Zisserman, "Very deep convolutional networks for large-scale image recognition," in *ICLR*, 2015.
- [3] C. Szegedy, W. Liu, Y. Jia, P. Sermanet, S. Reed, D. Anguelov, D. Erhan, V. Vanhoucke, and A. Rabinovich, "Going deeper with convolutions," in *CVPR*, 2015.
- [4] K. He, X. Zhang, S. Ren, and J. Sun, "Deep residual learning for image recognition," in *CVPR*, 2016.
- [5] G. Huang, Z. Liu, L. van der Maaten, and K. Q. Weinberger, "Densely connected convolutional networks," in *CVPR*, 2017.
- [6] L. Liu, C. Shen, L. Wang, A. van den Hengel, and C. Wang, "Encoding high dimensional local features by sparse coding based Fisher vectors," in *NIPS*, 2014.
- [7] Y. Gong, L. Wang, R. Guo, and S. Lazebnik, "Multi-scale orderless pooling of deep convolutional activation features," in *ECCV*, 2014.
- [8] M. Cimpoi, S. Maji, and A. Vedaldi, "Deep filter banks for texture recognition and segmentation," in *CVPR*, 2015.
- [9] O. Tuzel, F. Porikli, and P. Meer, "Region covariance: A fast descriptor for detection and classification," in *ECCV*, 2006.
- [10] J. Carreira, R. Caseiro, J. Batista, and C. Sminchisescu, "Free-form region description with second-order pooling," *IEEE TPAMI*, vol. 37, no. 6, pp. 1177–1189, 2015.
- [11] X. Pennec, P. Fillard, and N. Ayache, "A Riemannian framework for tensor computing," *IJCV*, vol. 66, no. 1, pp. 41–66, 2006.
- [12] V. Arsigny, P. Fillard, X. Pennec, and N. Ayache, "Fast and simple calculus on tensors in the Log-Euclidean framework," in *MICCAI*, 2005.
- [13] Q. Wang, P. Li, L. Zhang, and W. Zuo, "Towards effective codebookless model for image classification," *Pattern Recognition*, vol. 59, pp. 63–71, 2016.
- [14] D. G. Lowe, "Distinctive image features from scale-invariant keypoints," *IJCV*, vol. 60, no. 2, pp. 91–110, 2004.
- [15] P. Li, Q. Wang, H. Zeng, and L. Zhang, "Local Log-Euclidean multivariate Gaussian descriptor and its application to image classification," *IEEE TPAMI*, vol. 39, no. 4, pp. 803–817, 2017.
- [16] H. Jégou, F. Perronnin, M. Douze, J. Sánchez, P. Pérez, and C. Schmid, "Aggregating local image descriptors into compact codes," *IEEE TPAMI*, vol. 34, no. 9, pp. 1704–1716, 2012.
- [17] J. Sanchez, F. Perronnin, T. Mensink, and J. Verbeek, "Image classification with the Fisher vector: Theory and practice," *IJCV*, vol. 105, no. 3, pp. 222–245, 2013.
- [18] C. Ionescu, O. Vantzos, and C. Sminchisescu, "Matrix backpropagation for deep networks with structured layers," in *ICCV*, 2015.
- [19] T.-Y. Lin, A. RoyChowdhury, and S. Maji, "Bilinear CNN models for fine-grained visual recognition," in *ICCV*, 2015.
- [20] M. J. Daniels and R. E. Kass, "Shrinkage estimators for covariance matrices," *Biometrics*, vol. 57, no. 4, pp. 1173–1184, 2001.
- [21] D. L. Donoho, M. Gavish, and I. M. Johnstone, "Optimal shrinkage of eigenvalues in the spiked covariance model," *arXiv*, vol. 1311.0851, 2014.
- [22] Q. Wang, P. Li, W. Zuo, and L. Zhang, "RAID-G: Robust estimation of approximate infinite dimensional Gaussian with application to material recognition," in *CVPR*, 2016.
- [23] C. Stein, "Lectures on the theory of estimation of many parameters," *Journal of Soviet Mathematics*, vol. 34, no. 1, pp. 1373–1403, 1986.
- [24] O. Ledoit and M. Wolf, "A well-conditioned estimator for large-dimensional covariance matrices," *J. Multivariate Analysis*, vol. 88, no. 2, pp. 365–411, 2004.
- [25] L. Dryden, A. Koloydenko, and D. Zhou, "Non-Euclidean statistics for covariance matrices, with applications to diffusion tensor imaging," *The Annals of Applied Statistics*, 2009.
- [26] T.-Y. Lin and S. Maji, "Improved bilinear pooling with CNNs," in *BMVC*, 2017.
- [27] Q. Wang, P. Li, and L. Zhang, "G²DeNet: Global Gaussian distribution embedding network and its application to visual recognition," in *CVPR*, 2017.
- [28] P. Li, J. Xie, Q. Wang, and W. Zuo, "Is second-order information helpful for large-scale visual recognition?" in *ICCV*, 2017.
- [29] N. J. Higham, *Functions of Matrices: Theory and Computation*. Philadelphia, PA, USA: Society for Industrial and Applied Mathematics, 2008.
- [30] S. Xie, R. B. Girshick, P. Dollár, Z. Tu, and K. He, "Aggregated residual transformations for deep neural networks," in *CVPR*, 2017.
- [31] P. Li, J. Xie, Q. Wang, and Z. Gao, "Towards faster training of global covariance pooling networks by iterative matrix square root normalization," in *CVPR*, 2018.
- [32] A. Vedaldi and K. Lenc, "Matconvnet – convolutional neural networks for MATLAB," in *ACM on Multimedia*, 2015.
- [33] J. Deng, W. Dong, R. Socher, L.-J. Li, K. Li, and L. Fei-Fei, "ImageNet: A large-scale hierarchical image database," in *CVPR*, 2009.
- [34] B. Zhou, À. Lapedriza, A. Khosla, A. Oliva, and A. Torralba, "Places: A 10 million image database for scene recognition," *IEEE TPAMI*, vol. 40, no. 6, pp. 1452–1464, 2018.
- [35] C. Wah, S. Branson, P. Welinder, P. Perona, and S. Belongie, "The Caltech-UCSD Birds-200-2011 Dataset," Tech. Rep., 2011.
- [36] S. Maji, J. Kannala, E. Rahtu, M. Blaschko, and A. Vedaldi, "Fine-grained visual classification of aircraft," Tech. Rep., 2013.
- [37] J. Krause, M. Stark, J. Deng, and L. Fei-Fei, "3D object representations for fine-grained categorization," in *Workshop on 3D Representation and Recognition, ICCV*, 2013.
- [38] M. Cimpoi, S. Maji, I. Kokkinos, S. Mohamed, and A. Vedaldi, "Describing textures in the wild," in *CVPR*, 2014.
- [39] A. Quattoni and A. Torralba, "Recognizing indoor scenes," in *CVPR*, 2009.
- [40] Y. Gao, O. Beijbom, N. Zhang, and T. Darrell, "Compact bilinear pooling," in *CVPR*, 2016.
- [41] S. Kong and C. Fowlkes, "Low-rank bilinear pooling for fine-grained classification," in *CVPR*, 2017.
- [42] X. Dai, J. Yue-Hei Ng, and L. S. Davis, "FASON: First and second order information fusion network for texture recognition," in *CVPR*, 2017.
- [43] Y. Cui, F. Zhou, J. Wang, X. Liu, Y. Lin, and S. Belongie, "Kernel pooling for convolutional neural networks," in *CVPR*, 2017.
- [44] S. Cai, W. Zuo, and L. Zhang, "Higher-order integration of hierarchical convolutional activations for fine-grained visual categorization," in *ICCV*, 2017.
- [45] T. G. Kolda and B. W. Bader, "Tensor decompositions and applications," *SIAM Review*, vol. 51, no. 3, pp. 455–500, 2009.
- [46] Y. Li, N. Wang, J. Liu, and X. Hou, "Factorized bilinear models for image recognition," in *ICCV*, 2017.
- [47] Y. Wang, L. Xie, C. Liu, S. Qiao, Y. Zhang, W. Zhang, Q. Tian, and A. Yuille, "SORT: Second-order response transform for visual recognition," in *ICCV*, 2017.
- [48] R. Arandjelovic, P. Gronat, A. Torii, T. Pajdla, and J. Sivic, "NetVLAD: CNN architecture for weakly supervised place recognition," in *CVPR*, 2016.
- [49] P. Tang, X. Wang, B. Shi, X. Bai, W. Liu, and Z. Tu, "Deep FisherNet for object classification," *arXiv*, vol. abs/1608.00182, 2016.
- [50] Y. Li, M. Dixit, and N. Vasconcelos, "Deep scene image classification with the MFAFVNet," in *ICCV*, 2017.
- [51] M. Dixit and N. Vasconcelos, "Object based scene representations using fisher scores of local subspace projections," in *NIPS*, 2016, pp. 2811–2819.
- [52] E. Yang, A. Lozano, and P. Ravikumar, "Elementary estimators for sparse covariance matrices and other structured moments," in *ICML*, 2014.
- [53] Y. Chen, A. Wiesel, Y. C. Eldar, and A. O. Hero, "Shrinkage algorithms for MMSE covariance estimation," *IEEE TSP*, vol. 58, no. 10, pp. 5016–5029, 2010.
- [54] C. Ionescu, O. Vantzos, and C. Sminchisescu, "Training deep networks with structured layers by matrix backpropagation," *arXiv*, vol. abs/1509.07838, 2015.
- [55] L. T. Skovgaard, "A Riemannian geometry of the multivariate normal model," *Scand. J. Stat.*, vol. 11, no. 4, pp. 211–223, 1984.

- [56] S. Ioffe and C. Szegedy, "Batch normalization: Accelerating deep network training by reducing internal covariate shift," in *ICML*, 2015.
- [57] M. Lin, Q. Chen, and S. Yan, "Network in network," in *ICLR*, 2014.
- [58] J. Hu, L. Shen, and G. Sun, "Squeeze-and-excitation networks," in *CVPR*, 2018.
- [59] C. Woo, J. Park, J.-Y. Lee, and I. S. Kweon, "BAM: Convolutional block attention module," in *ECCV*, 2018.
- [60] K. Chatfield, K. Simonyan, A. Vedaldi, and A. Zisserman, "Return of the devil in the details: Delving deep into convolutional nets," in *BMVC*, 2014.
- [61] M. D. Zeiler and R. Fergus, "Visualizing and understanding convolutional networks," in *ECCV*, 2014.
- [62] P. Sermanet, D. Eigen, X. Zhang, M. Mathieu, R. Fergus, and Y. LeCun, "Overfeat: Integrated recognition, localization and detection using convolutional networks," in *ICLR*, 2014.
- [63] K. He, X. Zhang, S. Ren, and J. Sun, "Delving deep into rectifiers: Surpassing human-level performance on ImageNet classification," in *ICCV*, 2015.
- [64] T. Lin, A. Roy Chowdhury, and S. Maji, "Bilinear convolutional neural networks for fine-grained visual recognition," *IEEE TPAMI*, vol. 40, no. 6, pp. 1309–1322, 2018.
- [65] H. Zhang, J. Xue, and K. J. Dana, "Deep TEN: texture encoding network," in *CVPR*, 2017.
- [66] S. Ren, K. He, R. B. Girshick, and J. Sun, "Faster R-CNN: towards real-time object detection with region proposal networks," *IEEE TPAMI*, vol. 39, no. 6, pp. 1137–1149, 2017.
- [67] E. Shelhamer, J. Long, and T. Darrell, "Fully convolutional networks for semantic segmentation," *IEEE TPAMI*, vol. 39, no. 4, pp. 640–651, 2017.